Large eddy simulation of lithium-ion battery vent gases flame ignition and anchoring

Antony Cellier[a,*], Florent Duchaine[a], Thierry Poinsot[a,b], Emilien Brodu[c],
Bastien Boust[c], Marc Bellenoue[c], Gizem Okyay[d], Matthieu Leyko[d], Maxime Pallud[e]

[a]*CERFACS, 42 avenue Gaspard Coriolis, 31057 Toulouse, France*
[b]*Institut de Mécanique des Fluides de Toulouse, IMFT, Université de Toulouse, CNRS, Toulouse, France*
[c]*Institut P', 1 avenue Clément Ader, 86961 Futuroscope Chasseneuil, France*
[d]*SAFT Batteries, 111 Boulevard Alfred Daney, 33074 Bordeaux, France*
[e]*TotalEnergies - OneTech, 92400 Courbevoie, France*

Abstract

With the promotion of sustainable energy sources and electric mobility, reliable multi-scale storage systems become essential. Lithium-ion batteries are the preferred solution in most domains. However, when misused, lithium-ion batteries can trigger thermal runaway, self-heating reactions producing hot flammable and toxic gases. In order to better understand flame dynamics of battery-induced fires and explosions, a diagnosed experimental setup is built to mimic the high pressure-high temperature venting phase using synthetic vent gases, and offers validation operating points relevant to thermal runaway. The pre-heated jet fueled with vent gases allows to develop a methodology to assert ignition-extinction behavior and evaluate fire properties of given failing lithium-ion cells. It enables to validate a large eddy simulation framework able to reproduce the ignition sequence of the jet flame. Such an experimental-numerical approach gives space to study safety design choices and select promising vent strategy under controlled 3D simulation scenarios. It is a step towards a larger use of flow simulation during prototyping phases of safer battery designs, minimizing its cost and ensuring faster convergence towards the optimal.

Keywords: Lithium-ion cell fire, Thermal Runaway, Flame anchoring, Large Eddy Simulation

1) Novelty and Significance Statement

To fight the lack of information on lithium-ion cell fires, hardly reproducible and where imaging is difficult, a new experimental setup is presented. It consists in a pre-heated jet of combustible vent gases. Conditions representative of cell opening allow to validate both simulations of the high pressure jet leading to diamond shock structures, and simulations of flame ignition to anchoring. In this study, the focus is on the latter one. Using burner data, a large eddy simulation of the ignition sequence can be validated against experimental results. It motivates the use of such simulations to assert flame dynamics around given cell designs, helping to prepare efficient countermeasures.

2) Author Contributions

- A.C. designed research, performed simulation, analyzed data and wrote the paper
- F.D. designed research, analyzed data, and wrote the paper
- T.P. designed research, analyzed data, and wrote the paper
- E.B. performed experiments, and analyzed data
- B.B. designed research, performed experiments, analyzed data, and wrote the paper
- M.B. designed research, performed experiments, and analyzed data
- G.O. designed research
- M.L. designed research
- M.P. designed research

1. Introduction

The increase in production and use of lithium-ion (Li-ion) batteries drives the occurrence of statistically rare Thermal Runaway (TR) events [1]. Following an internal short-circuit generally triggered by misuse, cell components decompose into hot flammable and toxic gases. When vented out, the flammable gases can lead to combustion when conditions are met. Shocks when the cell opens, flames, explosions during or after gas venting, and heat propagation throughout the entire TR event are key combustion phenomena to study and eventually mitigate. Experimentally validated simulations of Li-ion batteries related fires could become a tool for the design of safer storage devices.

The reproduction of the phases of TR in a controlled environment is difficult using real cells, due to the highly statistical behavior of such systems under abuse conditions [2, 3]. Replicability is not guaranteed, flow parameters are difficult to obtain (mass-flow, mixture, temperature, ...), and comprehensive diagnostics are generally out of reach. There is thus a need for diagnosed Li-ion vent gases related jet flames, which would complete the recent will to apply Computational Fluid Dynamics (CFD), including combustion processes, to Li-ion venting and fires [4, 5]. Outside of the context of Li-ion, the study of jet flames is a core combustion topic. Flame dynamics starting from ignition, to stabilization or blow-off have been an experimental challenge in the past decades [6, 7]. After a successful ignition, the role of the triple flame on anchoring or stable lifting processes is key [7–9], motivating numerical [10, 11] and experimental [8, 12] studies on this special object in laminar and turbulent flows. It leads to a better understanding of the conditions necessary to obtain anchored, lifted or blown-off flames. The mechanisms have then been reproduced using CFD simulations to propose predictive tools regarding safety and performance of generations of combustors. Simulations validated versus experiments of free jet, jet in co-flow, or piloted jet flames with complete diagnostics are found in the literature. Considering the characteristic size and timing of the events, Large Eddy Simulation (LES) is often preferred for complete ignition scenarios. For example, reproductions of the Sandia piloted flames [13, 14] compose common benchmarks for CFD approaches [15, 16], completed by the Ahmed and Mastorakos jet in co-flow flame [17, 18].

In the specific domain of lithium-ion cells venting and fires, proper prototyping jet flames are still to be proposed, ensuring repeatability while mimicking Li-ion TR conditions. Those conditions are constraints to incorporate in the specifications of a Li-ion dedicated test bed. First, cell opening happens under high pressure [19] and is followed by the formation of an under-expanded jet so that high-pressure-driven venting must be ensured by the test bed. Then, the internal exothermic decomposition reactions induce high temperatures during venting, demanding for gas pre-heating. Lastly, a strong variability in mixture composition has already been identified [20]. Being able to test different mixtures is of first importance. Knowing these constraints, an experimental setup is proposed as a platform to compare to simulation under relevant, well controlled flow conditions, and elucidate the flame stabilization mechanisms at play in this original situation. A validation operating point consisting in the ignition sequence of the jet flame is selected. It serves as reference for reactive LES of this Li-ion specific jet flame ignition sequence.

2. Experimental setup

2.1. System and diagnostics

Figure 1 gives an overall description of the Battery Thermal Runaway (BTR) setup installed at the Pprime institute. It consists in a pre-heated jet driven by a pressurized tank. To reproduce the critical venting conditions, three main parameters are controlled: pressure, temperature and mixture composition.
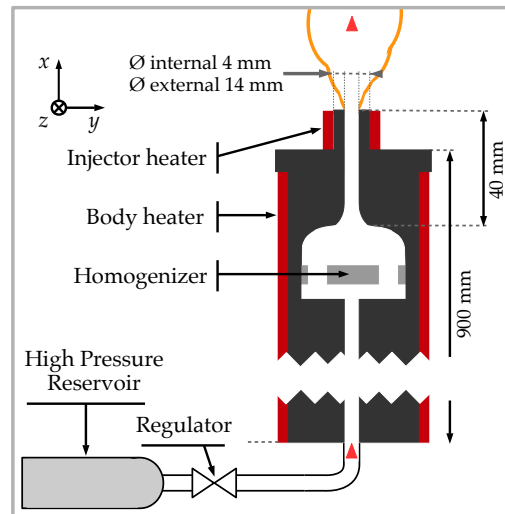

Fig. 1: Description of the BTR experimental setup.

Pressure and mixture inside the reservoir can be modified to fit different venting conditions. A driving pressure up to $1.25\,\mathrm{MPa}$ can be set inside the reservoir allowing at least $0.5\,\mathrm{MPa}$ inside the homogenization chamber. Once released from the reservoir, gases pass a $900\,\mathrm{mm}$-long tube surrounded by annular body heaters optimized to guarantee a vented flow temperature above $1000\,\mathrm{K}$. It is supplemented by an injector heater to counteract thermal losses. To add turbulence, the homogenization chamber features a $12\,\mathrm{mm}$ thick homogenizer plate pierced with six holes, $5\,\mathrm{mm}$ in diameter. The injector internal diameter reduces to $4\,\mathrm{mm}$, to approximate 18650-type cells venting holes typical design [19]. The external diameter is $14\,\mathrm{mm}$, offering a hot surface to test flame anchoring and auto-ignition for highly reactive mixtures

3

(e.g. pure hydrogen). Multiple pressure and temperature sensors monitor the state of the system: seven Druck UNIK 5000 pressure sensors are associated with type K thermocouple temperature probes (see Fig. 2). In addition to the sensors at the reservoir outlet (P_0, T_0), (P_1, T_1) to (P_5, T_5) document the heating process and pressure loss. Conditions inside the homogenization chamber, after the homogenizer, are retrieved by (P_6, T_6). Three sensors T_{inj}, T_{w1}, T_{w2} record the solid temperatures inside the body and at the injector lips. A Coriolis flow meter completes the sensor setup, located at the pressurized reservoir. Jet and flame imaging is obtained through two cameras, depending on the flow specificity to assert. Shocks are recorded by shadowgraph imaging using a high-speed camera (Photron SA-Z, 12 bit). Flame imaging is based on broadband chemiluminescence (Phantom V310, 3×8 bit). To test forced ignition, a Beru ZSE030 spark ignitor is used and placed 10 mm above the injector, setup to deliver an impulse every 20 ms.

Fig. 3: Operating the BTR setup: a) succession of events during a test with the evolution of P_5, b) Spark ignitor voltage command.

Fig. 4: Pressure and temperature sensor acquisition for a complete venting procedure.

2.2. Test bed operation

Figure 3 and 4 summarize the key phases of a test. The pressurized reservoir is opened at $t = 0$ s and its content is rapidly released, creating a sudden pressurization of the system, followed by a slow expansion. In less than one second, pressure sensors P_1 to P_6 reach a peak where a diamond shock-expansion
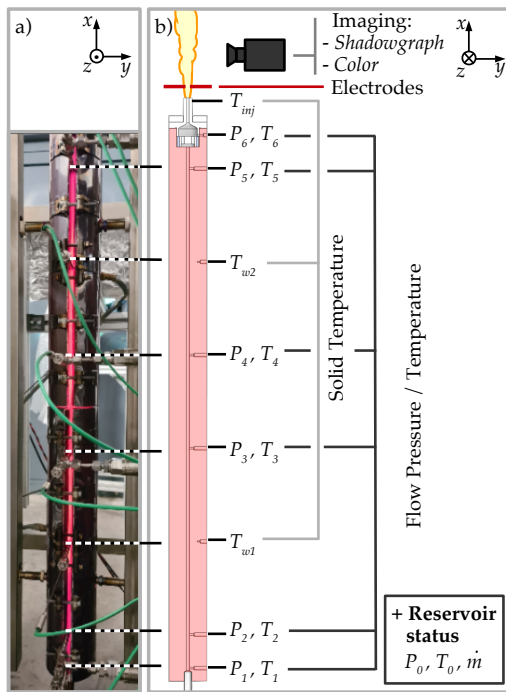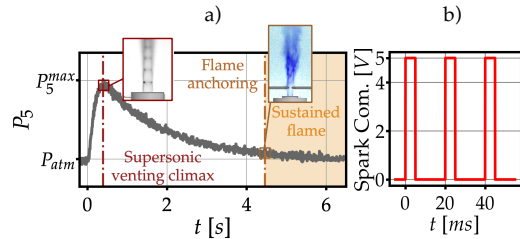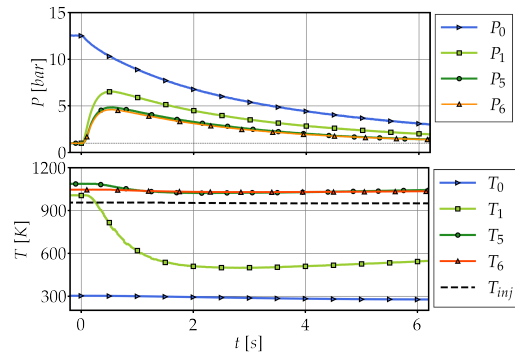

Fig. 2: Illustration of the diagnostics location: a) Photograph of the body with probe locations, b) Description of all the diagnostics, located on the schematic of the system.

structure forms at the injector lips. After the supersonic venting climax, a time lapse is needed so that the mass-flow reduces and meets values where a successful ignition triggered by the spark ignitor can be obtained. It is followed by flame anchoring and stabilization. The two operating points identified as the "supersonic venting climax" (representative of cell opening and supersonic jet formation) and the "flame anchoring" (representative of cell-level flame ignition and sustained fire) are key to obtain experimental information on a given vent gas mixture at relevant venting conditions. They serve as reference points for the validation of a 3D simulation platform.

2.3. Operating point selection

The validation of the simulation setup is divided into two cases: 1. Inert supersonic jets are asserted to reproduce properly the succession of diamond shock structures. Also, it helps to validate the simulation setup for cell-level safety opening and overpressure venting, 2. Spark ignition of the vent gas plume, with the succession of events leading to flame anchoring. This paper focuses on the second case.

The target for this study is the course of events leading to the presence of a flame anchored at the lips of the injector for the Li-ion vent mixture sampled in [2] (% in volume): H_2: 30.8 %, CH_4: 6.8 %, C_2H_4: 8.2 %, CO: 13.0 %, CO_2: 41.2 %.The sample originates from an overheat-to-TR test performed on a batch of fully-charged 18650 cells. Cathode ma-
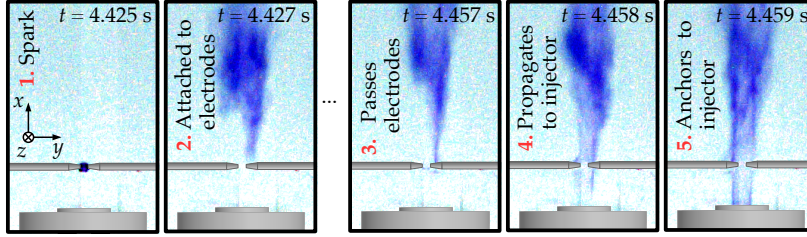
4

Fig. 5: Experimental rapid camera imaging of the flame anchoring phases for the selected operating point.

terial is $Li(Ni_{0.45}Mn_{0.45}Co_{0.10})O_2$ and the atmosphere is flushed with Argon to avoid oxidation before sampling. bottles of the mixture are ducted to the system, allowing repeated testing under identical conditions. To experimentally evaluate the level of repeatability of a venting followed by ignition and anchoring, three different initial reservoir pressure P_0 are selected: 0.20, 0.25, 0.30 MPa. The homogenization chamber driving overpressure $\Delta P_6^{ign} = P_6^{ign} - P_{amb}$ is measured at the instant of flame anchoring for the three venting. The maximum error relative to the average value of ΔP_6^{ign} is 16.7%. Repeated venting thus deliver similar conditions at the instant of successful ignition, helping to select one venting as a reference to compare with simulation.

The event can be summarized as follows. Starting from a reservoir pressure $P_0 = 0.3$ MPa, a body pre-heating temperature of 1073 K, and an injector pre-heating temperature of 963 K, a venting procedure is launched. During venting, the ignition system is triggered every 20 ms, until successful ignition. First, the mass-flow rapidly increases reaching its maximum at climax with a value of 2.4 g.s^{-1}. As reservoir pressure progressively decreases, the mass-flow is reduced. Following multiple unsuccessful ignition, at $t = t_{ign} = 4.425$ s, conditions are finally met and a spark ignites a flame that first anchors to the electrodes and eventually propagates towards the injector to anchor at the lips at $t = t_{anc} = 4.459$ s. Considering the short duration of the whole sparking-to-anchoring sequence (under 50 ms) with respect to the complete venting procedure (10 s), driving conditions are assumed constant. It is confirmed by the measurement of the mass-flow, varying by less than 3 % on this short period of time. Figure 5 depicts the succession of events leading to anchoring[1].

2.4. Simulation objective definition

From an experimental versus simulation validation point of view, three successive flame regimes are expected (see Fig. 5). The first one follows ignition and kernel propagation. It is the partially premixed

flame stabilized at the electrodes, waiting for conditions sufficient to pass them. The second one is the flame anchoring phase after the crossing of the electrode. In this section, the low turbulence and the absence of mixing are suitable for the observation of a triple flame [8, 10, 12] propagating towards the lips. This event is timed using camera imaging (3-4 ms) and helps to assert the timescales to reproduce using simulation. Eventually, the anchored jet diffusion flame topology formed by a first tubular quasi-laminar flame attached to the lip up to the electrodes, topped with a turbulent partially premixed plume flame is also of interest when comparing simulation to experiment. Both flame topologies and transition timing are therefore to be reproduced. It helps to reveal forces and weaknesses of the framework in each phase. One crucial mechanism is the triple flame propagation, essential to assert flame anchoring in further applications, and a special care will be given to this section.

3. Simulation framework

3.1. Geometry, mesh and boundary conditions

For the simulation, the geometry is cut at the plane (P_5, T_5) where information is sufficient to prescribe correct inlet quantities. Starting at (P_5, T_5), it contains the homogenization structure, the nozzle and the injector. (P_6, T_6) helps to verify that conditions given at (P_5, T_5) fit experimental values. The entire domain considered for simulation is given in Fig. 6 a) and consists in a cylinder of 900 mm in length and 1000 mm in diameter so that the jet streams in an open atmosphere. Mesh refinement inside the system is summarized in Fig. 6 b). It guarantees 20 points in the diameter of the final injector tube ($\Delta x = 0.2$ mm) and more than 15 points in the feeding channels. Figure 6 c) shows that mesh refinement at the jet foot is imposed to be $\Delta x = 0.2$ mm. The choice is motivated by the fact that it enables at least ten points in the width of a representative 1D laminar counter-flow diffusion flame [21, 22]. The refinement relaxes to $\Delta x = 0.7$ mm after a distance $x/D = 15$, for the jet plume. The mesh totals 32.4 M tetrahedrons.

Concerning boundary conditions of the cylindrical domain, the back plane is modeled as an adiabatic wall and side walls are treated with slip conditions. The outlet of the domain is the upper surface of the cylinder, and the inlet is the (P_5, T_5)

---

[1] Phantom V310 set to 1000 frames per second, a 1280×304 resolution, with a 990 μs shutter speed (Ø 55 mm, F 100 mm, O f/2.8). Images are contrasted, inverted, and reset to blue for printing.
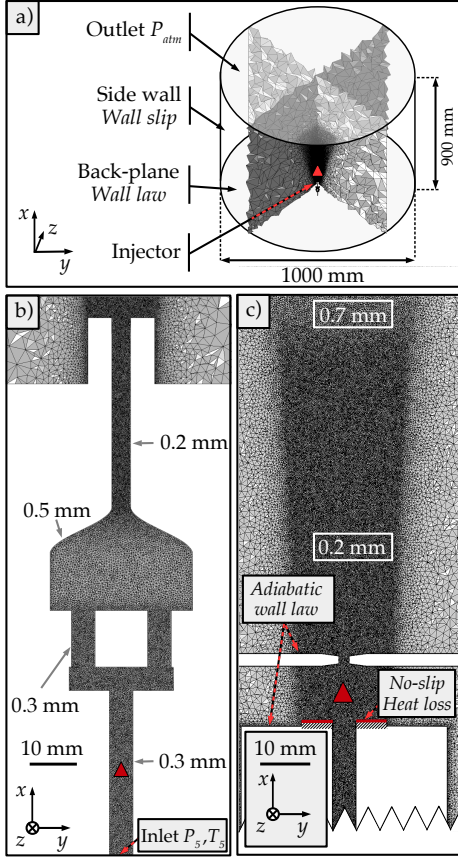
Fig. 6: Mesh of the simplified BTR test bed: a) overall view of the mesh through cuts, b) Zoom on a cut of the mesh inside the system, c) Refinement criteria inside the jet.

plane at the interface between the body heater and the homogenization chamber where conditions are imposed based on static pressure, static temperature and mixture fractions. Inlets and outlets are enforced using Navier-Stokes Characteristic Boundary Conditions (NSCBC) [23]. Adiabatic wall laws are selected for all internal boundary conditions, based on the fact that the body and injector heaters limit the heat losses and maintain total temperature close to constant, and that velocity conditions imply a normalized first wall cell size y^+ larger than 20 requiring wall modeling. The injector lips use no slip conditions with heat losses, to impose realistic temperature and surface thermal resistance in this low-velocity region where the flame is intended to anchor. The sensor data monitoring the sequence offers input parameters for the simulation of this ignition-to-anchoring phase. The corresponding operating point is given in Table 1. (P_5, T_5) defines the inlet, and (P_6, T_6) helps to validate simulation, along with reservoir mass-flow. A thermocouple measures the solid temperature $2.5\,\mathrm{mm}$ under the surface at $T_{lip} = 944\,\mathrm{K}$. Using an approximate of the thermal conductivity of the stainless steel

(17-4PH) at this temperature [24], the thermal resistance is evaluated: $R_{th} \simeq 1.14 \times 10^{-4}\,\mathrm{K.m^2.W^{-1}}$. Adiabatic wall laws are used for the electrodes, assuming that no heat is lost through them, given their small diameter and the repeated sparking leading to heating.

Table 1: Operating conditions during flame ignition and anchoring. Pressures are measured with respect to ambient.

Sensor position	$\cdot 5$	$\cdot 6$
ΔP (Pa)	2590.0	2210.0
T (K)	1093.0	1063.0
T_{lip} (K)		944.0
Reservoir mass-flow (g.s^{-1})		0.33

3.2. Reactive LES setup

In the framework of AVBP [25], to solve for the reactive Navier Stokes equations, two numerical schemes are tested: the Lax Wendroff scheme (LW) [26], second order in time and space, and the Two-step Taylor Galerkin scheme TTGC [27], third order, to see the effect of scheme order on the solution both in terms of aerodynamics (cold flow) and flame topology (ignition sequence). The subgrid scale model is WALE [28][2], CFL and Fourier numbers are 0.7 and 0.1 respectively in all cases. Numerical stability is enhanced by second-order and fourth-order artificial viscosity terms [29]. Chemical kinetics are modeled using an analytically reduced scheme [30] set and tested in [22] for high temperature premixed flames and high-temperature fuel against low-temperature air counterflow diffusion flames. The dynamically thickened flame for LES paradigm (DTFLES) [31] completes combustion modelling choices. The static Charlette efficiency formulation with a constant equal to 0.5 is chosen [32]. The thickening model is amended to deactivate in diffusion-dominated regions using the work of Yamashita et al. [33].

3.3. Cold flow initialization and ignition

Before ignition, using P_5/T_5 measurements as inlet conditions, a cold flow simulation is performed to assert effects of numerical schemes on turbulence and converge the jet before ignition. Following $150\,\mathrm{ms}$ of physical time simulation using LW, two simulations are computed for an additional $40\,\mathrm{ms}$ each. One continues with LW, the other uses TTGC. Given the reasonably well detailed mesh chosen due to combustion constraints, increasing the order of the numerical scheme only offers marginal improvements in this setup for this cold flow stabilization (see Fig. 7).

For ignition, the Energy Deposition model (ED) is selected [18]. The model allows to apply a spheri-

---

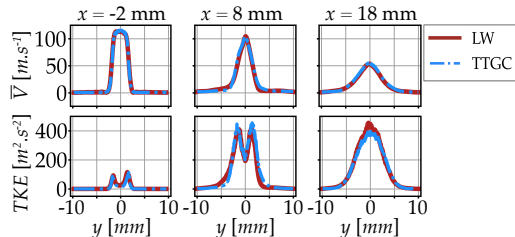[2]Turbulent Prandtl and Schmidt numbers are both equal to 0.6.

6

Fig. 7: Plot over line of $\overline{V}$ and Turbulent Kinetic Energy (TKE), 2 mm under the electrodes, 8 and 18 mm over the electrodes.

cal source term of energy, mimicking a spark ignitor, while controlling the total deposit in terms of energy, spatial distribution and timing. In this study, the spark ignitor is commanded to deliver impulses every 20 ms and a similar ignition device has been studied by Benito [34]. For air at atmospheric conditions, with an inter-electrode gap of 1.8 mm, the measured electrical and thermal energy at the electrode reach up to 50 mJ and 20 mJ respectively. In the experiment where the spark is triggered in hot flowing gases, no direct access to the energy deposited is available. Therefore, it has been chosen to set the minimum energy necessary for a successful ignition-to-anchoring procedure in simulation by incrementally reducing the command energy. The optimal energy is found at 50 mJ. Simulation spark properties can be summarized as a single 50 mJ total energy spherical source following a Gaussian profile in time ($\Delta t = 100\,\mu s$) and space ($\Delta x = 8.0$ mm).

4. Experimental versus simulation comparisons

4.1. Overview of the ignition procedure

Figure 8 shows the comparison between experimental contrasted photography and longitudinal cuts of the temperature field obtained by LES (TTGC) for the full ignition procedure. The main phases of ignition are highlighted. While the main aspects of the flame structure are qualitatively recovered, more details need to be put to interpret every section and its timing, which is the focus of the next sections. In particular, the timing of the whole procedure is very dependent on the phase of electrode anchoring, explaining the discrepancy between experimental and simulation. It is discussed in Section 4.2. A critical evaluation of the framework follows, and threads to go after are highlighted, for future improvements.

4.2. Electrode anchoring and blow-off prediction

After ignition, the flame stabilized over the electrodes waits for conditions sufficient to pass the electrodes. Experimentally, this phase lasts 30 ms, while it is largely underestimated by LES at only 1.2 ms. Interestingly, the timing of the kernel to early attached flame phase does not drift from the 1-2 ms ob-

served experimentally, and similarly, the electrode-to-injector flame propagation phase is well timed (see Sec. 4.3). It means that flame velocity, and flow velocity cannot be solely responsible for this order-of-magnitude difference. Two main hypotheses are thus formulated to understand why this behavior is observed. To begin with, in simulations, electrodes are modelled using adiabatic walls based on the fact that their diameter is low (2.0 mm), and the hot flow added to the successive sparking during 4.425 s preheats the tips. However, losses may exist and play the role of a retardant to the flame crossing the electrodes. Without a proper evaluation of experimental losses and surface temperature, asserting the thermal resistance is thorny. The use of coupling to solve the heat equation inside electrode tips may become the solution in such a configuration, and thus help to test this hypothesis. It is a promising way to increase the physical resemblance with experimental. Moreover, radiative losses may also be significant during the kernel formation, and while the flame propagates from electrodes to injector lips. It constitutes a second perspective: completing the coupling procedure with a radiative transfer equation solver. A second hypothesis is linked to the operating point in itself. The operating point selected is inherently close to blow-off limits as it is the first spark that successfully leads to ignition during a progressive decrease of mass-flow. Measurement uncertainties in unsteady pressure and temperature sensing may be responsible of slight variations of the mass-flow throughout the procedure, decreasing by a small percentage between the electrodes and the lip anchoring. This hypothesis can be tested by evaluating the sensitivity of LES to a small increase in mass-flow. The case at hand corresponds to an inlet mass-flow $\dot{m}^{sim} = 0.31$ g.s^{-1}. A second case is set with a 5% increase at $\dot{m}^{sim} = 0.326$ g.s^{-1}. Figure 9 compares the two ignition sequences. A complete blow-off is observed at a 5% higher mass-flow, giving two pieces of information. On the one hand, the experimental operating point, during the electrode-anchored flame sequence, may be located in-between the two cases, delaying the electrode to lip anchoring. On the other hand, assuming that this operating point is close to blow-off, LES is capable to contour the frontier of blow-off of such a configuration. It ensures a better applicability to real use-cases such as the one proposed in [22].

Overall, this section emphasizes one limitation of the selected framework in the timing of the electrode-anchored flame. While the operating point definition may be in cause, it opens the path to a future evaluation of a coupled simulation taking into account losses in the electrodes, to fully close the hypothesis. It is important to note that a similar behavior is observed for both numerical schemes. Eventually, once conditions are suited in simulation and experimental, the flame crosses electrodes and a triple flame forms and propagates towards the lips, which is a key phenomenon to cover in order to predict flame anchoring or blow-off in other applications.
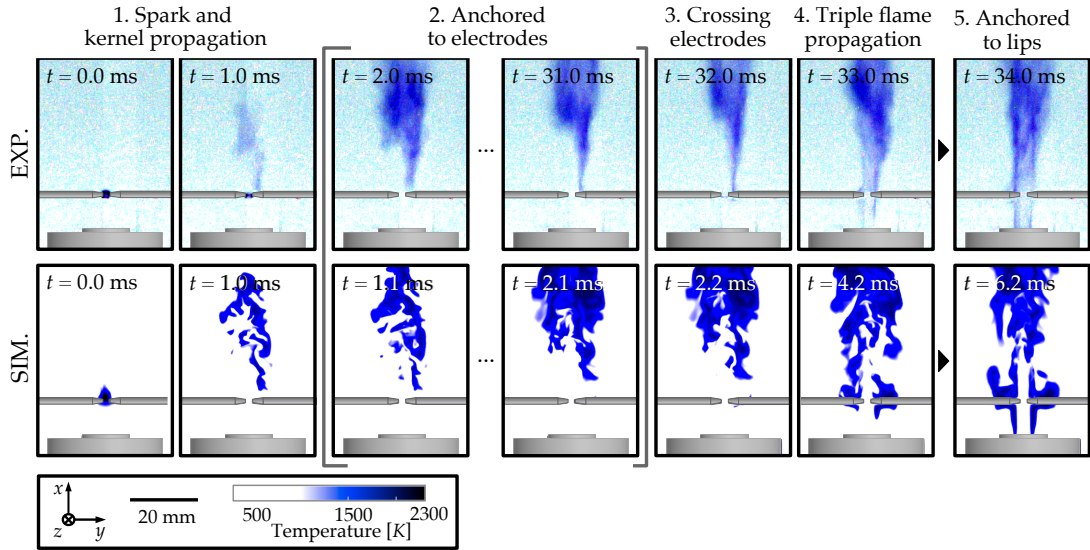
7

Fig. 8: Experimental versus simulation comparison of the three phases of the ignition-to-anchoring procedure (using TTGC). Experimental views correspond to contrasted photography of the flame, simulation views show z-normal cuts of the temperature field.
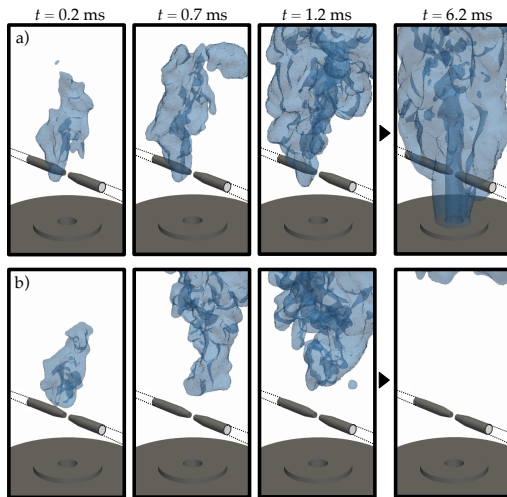

Fig. 9: Effect of mass-flow on the ignition procedure outlined as 3D contour of HRR using TTGC (iso-level HRR.F = 1×10^7 J.m^{-3}.s^{-1}): a) $\dot{m}^{sim} = 0.31$ g.s^{-1}, b) $\dot{m}^{sim} = 0.326$ g.s^{-1}.

4.3. Electrode to lip anchoring

Triple flames appear in presence of gradients of mixture fraction [8], where diffusion jet flame ignition is a special case. A triple flame controls the jet flame lifted stabilization [17] and defines anchoring processes if conditions are met. Their reproduction using DTFLES becomes a crucial test-case for simulation setups [18]. Starting from the electrode, and from a 2D-cut perspective, the three flame branches form, one rich premixed, one diffusion and one lean premixed. Once formed, the structure propagates upstream following the stoichiometric line, depending on local axial velocity conditions. A cut of the flame showing the leading point is given in Fig. 10. At the time where the leading point of the flame touches the lips, the tubular diffusion flame is fully formed. To better follow the timing of this phase, the flame leading point is tracked. The time of anchoring is set to the time at which the flame touches the lip of the injector. In Fig. 11, the position of the flame front with respect to the lip is reported. Available experimental points are added. Knowing that a certain uncertainty exists to determine precisely the exact time of electrode crossing, the agreement with both TTGC and LW simulation setups is acceptable.
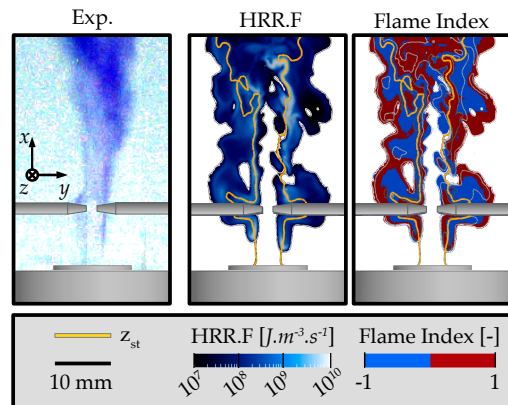

Fig. 10: Triple flame propagation as z-normal cuts of normalized heat release rate (HRR.F) and flame index compared to experimental 1 ms before anchoring.
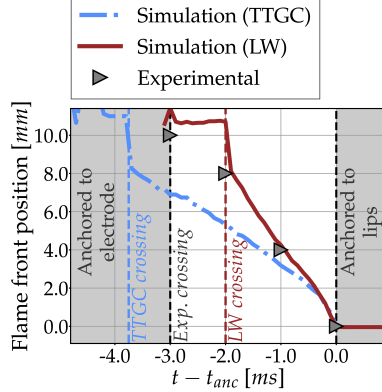
Fig. 11: Comparison of flame positions with respect to the lips during the anchoring phase using TTGC and LW.

4.4. Application to 18650 cell design

A scenario of flame ignition around a 18650 cell is proposed as a direct application of this study. Using the setup and scenario created in [22], a comparison between a five venting holes design and a three venting holes design is done. Results extensively discussed in [35] are summarized in Fig. 12. It shows that under the same conditions at ignition, the use of a three-hole vent cap will tend to a rapid blow-off. From an industrial point of view, such simulations create design guidelines, where it can be chosen a priori whether it is preferable to favor ignition and anchoring (strong heat generation) or blow-off (giving space to delayed ignition and explosion scenarios). The vent gas mixture can also be changed to account for the internal material of the cell, changing outcomes, as presented in [35].

5. Conclusion

An experimental setup is introduced to target operating points representative of the venting of Li-ion cells, consecutive to TR. Diagnostics allow simulation-experimental comparisons to validate choices in terms of computation paradigm and models. The LES framework proposed here gives the opportunity to perform ignition procedures and assert strengths and weaknesses of state-of-the-art methodologies on Li-ion related fires. After a cold flow simulation using two numerical schemes, the phases of ignition are presented and reproduced. In particular, the triple flame propagation timing and the sensitivity to blow-off are retrieved, opening the path to an application to realistic cases. LES correctly predicts ignition timing and flame displacement, confirming its capability to reproduce the phenomenon in this special configuration dedicated to hot Li-ion vent gases.

Such an experimental setup gives the opportunity to compare multiple operating points, reflecting the different states of a battery reaching TR. This state is translated to the mixture vented out, which changes
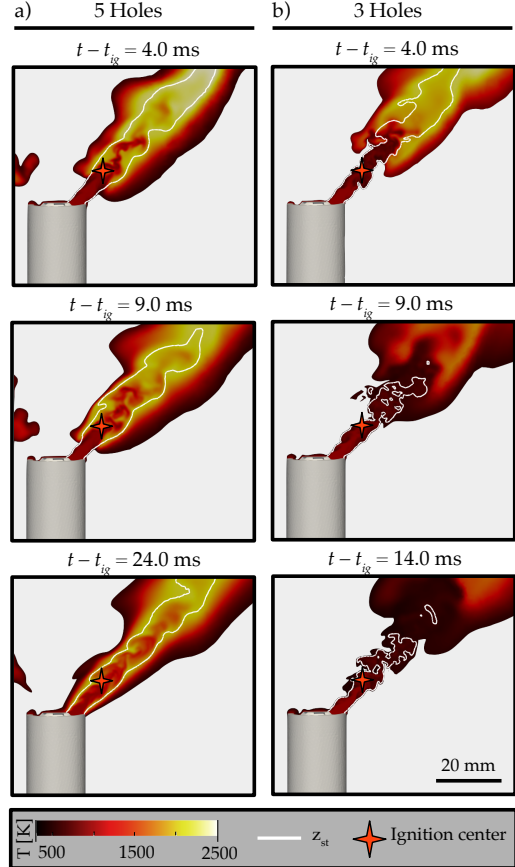

Fig. 12: Flame ignition-extinction behavior for two 18650 cell design following the same scenario: a) five-holes design, b) three-holes design.

based on the State of Charge, the aging, the type of TR trigger, ... These considerations can be included using different fueling bottles, prepared for each conditions, along with various venting pressures, temperatures, ignitor height and frequency.

Concerning the simulation setup, a broader parameter variation is to be performed, to ensure further validation. In particular, improving the spark ignitor model is one key extension to aim at, along with the influence of liquid and solid ejection on ignition sequences. Nonetheless, thanks to this numerical tool, it becomes possible to assert the effect of design guidelines regarding vent caps of lithium-ion cells. Defining scenarios and comparing structural choices in terms of fire response is an ongoing work, helping to get closer to Li-ion manufacturer concerns, offering a simulation strategy to reach environmental-aware and cost-efficient prototyping steps.

Declaration of competing interest

The authors declare that they have no known competing financial interests or personal relationships that

9

could have appeared to influence the work reported in this paper.

Acknowledgments

References

[1] X. Feng, M. Ouyang, X. Liu, L. Lu, Y. Xia, X. He, Thermal runaway mechanism of lithium ion battery for electric vehicles: A review, Energ. Storage Mater. 10 (2018) 246–267.

[2] A. W. Golubkov, D. Fuchs, J. Wagner, H. Wiltsche, C. Stangl, G. Fauler, G. Voitic, A. Thaler, V. Hacker, Thermal-runaway experiments on consumer Li-ion batteries with metal-oxide and olivin-type cathodes, RSC Adv. 4 (2014) 3633–3642.

[3] A. García, J. Monsalve-Serrano, R. Lago Sari, S. Martinez-Boggio, An optical investigation of thermal runway phenomenon under thermal abuse conditions, Energ. Convers. Manage. 246 (2021) 114663.

[4] D. Kong, G. Wang, P. Ping, J. Wen, A coupled conjugate heat transfer and CFD model for the thermal runaway evolution and jet fire of 18650 lithium-ion battery under thermal abuse, eTransportation 12 (2022) 100157.

[5] W. Li, V. León Quiroga, K. R. Crompton, J. K. Ostanek, High Resolution 3-D Simulations of Venting in 18650 Lithium-Ion Cells, Front. Energ. Res. 9 (2021) 1–19.

[6] E. Mastorakos, Ignition of turbulent non-premixed flames, Prog. Energ. Combust. Sci. 35 (2009) 57–97.

[7] K. M. Lyons, Toward an understanding of the stabilization mechanisms of lifted turbulent jet flames: Experiments, Prog. Energ. Combust. Sci. 33 (2007) 211–231.

[8] P. N. Kioni, B. Rogg, K. N. Bray, A. Liñán, Flame spread in laminar mixing layers: The triple flame, Combust. Flame 95 (1993) 276–290.

[9] J. Buckmaster, Edge-flames, Prog. Energ. Combust. Sci. 28 (2002) 435–475.

[10] G. R. Ruetsch, L. Vervisch, A. Liñán, Effects of heat release on triple flames, Phys. Fluids 7 (1995) 1447–1454.

[11] C. Jiménez, B. Cuenot, DNS study of stabilization of turbulent triple flames by hot gases, Proc. Combust. Inst. 31 (2007) 1649–1656.

[12] L. Muñiz, M. G. Mungal, Instantaneous flame-stabilization velocities in lifted-jet diffusion flames, Combust. Flame 111 (1997) 16–30.

[13] R. S. Barlow, J. Frank, Effects of Turbulence on Species Mass Fractions in Methane/Air Jet Flames, Proc. Combust. Inst. (1998) 1087–1095.

[14] C. Schneider, A. Dreizler, J. Janicka, E. P. Hassel, Flow field measurements of stable and locally extinguishing hydrocarbon-fuelled jet flames, Combust. Flame 135 (2003) 185–190.

[15] H. Pitsch, H. Steiner, Large-eddy simulation of a turbulent piloted methane/air diffusion flame (Sandia flame D), Phys. Fluids 12 (2000) 2541–2554.

[16] S. Zadsirjan, S. Tabejamaat, E. Abtahizadeh, J. van Oijen, Large eddy simulation of turbulent diffusion jet flames based on novel modifications of flamelet generated manifolds, Combust. Flame 216 (2020) 398–411.

[17] S. F. Ahmed, E. Mastorakos, Spark ignition of lifted turbulent jet flames, Combust. Flame 146 (2006) 215–231.

[18] G. Lacaze, E. Richardson, T. Poinsot, Large eddy simulation of spark ignition in a turbulent methane jet, Combust. Flame 156 (2009) 1993–2009.

[19] F. Austin Mier, M. J. Hargather, S. R. Ferreira, Experimental Quantification of Vent Mechanism Flow Parameters in 18650 Format Lithium Ion Batteries, J. Fluids Eng. 141 (2019) 1–11.

[20] A. R. Baird, E. J. Archibald, K. C. Marr, O. A. Ezekoye, Explosion hazards from lithium-ion battery vent gas, J. Power Sources 446 (2020) 227257.

[21] B. Cuenot, F. Shum-Kivan, S. Blanchard, The thickened flame approach for non-premixed combustion: Principles and implications for turbulent combustion modeling, Combust. Flame 239 (2022) 111702.

[22] A. Cellier, F. Duchaine, T. Poinsot, G. Okyay, M. Leyko, M. Pallud, An analytically reduced chemistry scheme for large eddy simulation of lithium-ion battery fires, Combust. Flame 250 (2023) 112648.

[23] F. Nicoud, Defining Wave Amplitude in Characteristic Boundary Conditions, J. Comput. Phys. 149 (1999) 418–422.

[24] A. S. Sabau, W. D. Porter, Alloy shrinkage factors for the investment casting of 17-4PH stainless steel parts, Metal. Mater. Trans. B 39 (2008) 317–330.

[25] Cerfacs, AVBP CFD solver, available at https://www.cerfacs.fr/avbp7x/.

[26] P. Lax, B. Wendroff, Systems of conservation laws, Tech. rep. (1959).

[27] O. Colin, M. Rudgyard, Development of High-Order Taylor-Galerkin Schemes for LES, J. Comput. Phys. 162 (2000) 338–371.

[28] F. Nicoud, F. Ducros, Subgrid-scale stress modelling based on the square of the velocity, Flow Meas. Instrum. 62 (1999) 183–200.

[29] A. Jameson, W. Schmidt, E. Turkel, Numerical solution of the Euler equations by finite volume methods using Runge Kutta time stepping schemes, AIAA Fluid and Plasma Dynamics Conf. (1981).

[30] Q. Cazères, P. Pepiot, E. Riber, B. Cuenot, A fully automatic procedure for the analytical reduction of chemical kinetics mechanisms for Computational Fluid Dynamics applications, Fuel 303 (2021).

[31] O. Colin, F. Ducros, D. Veynante, T. Poinsot, A thickened flame model for large eddy simulations of turbulent premixed combustion, Phys. Fluids 12 (2000) 1843–1863.

[32] F. Charlette, C. Meneveau, D. Veynante, A power-law flame wrinkling model for LES of premixed turbulent combustion Part I: Non-dynamic formulation and initial tests, Combust. Flame 131 (2002) 159–180.

[33] H. Yamashita, M. Shimada, T. Takeno, A numerical study on flame stability at the transition point of jet diffusion flames, Proc. Combust. Inst. 26 (1996) 27–34.

[34] C. J. Benito Parejo, Experimental Characterization of Electrical Discharges and Formation of the Ignition Kernel. Application to the Study of Performances of Aeronautical Igniters, Ph.D. thesis, ISAE-ENSMA, Chasseneuil-du-Poitou (2019).

[35] A. Cellier, Large eddy simulation of lithium-ion battery fire for the diagnostic of thermal runaway, Ph.D. thesis, INPT, Toulouse (2023).